RESEARCH ARTICLE

NANO · MICRO small
www.small-journal.com

C_{60}-based Multivalent Glycoporphyrins Inhibit SARS-CoV-2 Specific Interaction with the DC-SIGN Transmembrane Receptor

Jennifer Patino-Alonso, Justo Cabrera-González, Javier Merino, Gema Nieto-Ortiz, Fátima Lasala, Jouma Katati, Carlos H. Bezerra da Cruz, Ajay K. Monnappa, Pablo Mateos-Gil, Ángeles Canales,* Iván López-Montero,* Beatriz M. Illescas,* Rafael Delgado,* and Nazario Martín**

Since WHO has declared the COVID-19 outbreak a global pandemic, nearly seven million deaths have been reported. This efficient spread of Severe Acute Respiratory Syndrome Coronavirus-2 (SARS-CoV-2) is facilitated by the ability of the spike glycoprotein to bind multiple cell membrane receptors. Although ACE2 is identified as the main receptor for SARS-CoV-2, other receptors could play a role in viral entry. Among others, C-type lectins such as DC-SIGN are identified as efficient trans-receptor for SARS-CoV-2 infection, so the use of glycomimetics to inhibit the infection through the DC-SIGN blockade is an encouraging approach. In this regard, multivalent nanostructures based on glycosylated [60]fullerenes linked to a central porphyrin scaffold have been designed and tested against DC-SIGN-mediated SARS-CoV-2 infection. First results show an outstanding inhibition of the trans-infection up to 90%. In addition, a deeper understanding of nanostructure-receptor binding is achieved through microscopy techniques, high-resolution NMR experiments, Quartz Crystal Microbalance experiments, and molecular dynamic simulations.

1. Introduction

The Severe Acute Respiratory Syndrome Coronavirus-2 (SARS-CoV-2) virus spread has caused the recent COVID-19 pandemic, which led to the death of more than 6.8 million people and more than 755 million confirmed cases.[1] Despite the main treatment through vaccination has efficiently protected population, the development of antivirals is also desirable, both to protect people who have already been infected and also to provide health systems of new and more efficient therapies.

Even though angiotensin converting enzyme 2 (ACE2) has been identified as the canonical receptor for carbohydrate binding domain (CRD) of SARS-CoV-2 spike protein,[2] ACE2-independent cell internalization has also been reported.[3]

J. Patino-Alonso, J. Cabrera-González, J. Merino, G. Nieto-Ortiz, Á. Canales, B. M. Illescas, N. Martín
Departamento de Química Orgánica
Facultad de Química
Universidad Complutense
Madrid E-28040, Spain
E-mail: justocab@ucm.es; ma.canales@quim.ucm.es; beti@quim.ucm.es; nazmar@ucm.es

The ORCID identification number(s) for the author(s) of this article can be found under https://doi.org/10.1002/smll.202307045

DOI: 10.1002/smll.202307045

J. Cabrera-González
Departamento de Química en Ciencias Farmacéuticas
Facultad de Farmacia
Universidad Complutense
Madrid E-28040, Spain

F. Lasala, A. K. Monnappa, P. Mateos-Gil, I. López-Montero, R. Delgado
Instituto de Investigación Biomédica Hospital 12 de Octubre (imas12)
Madrid 28041, Spain
E-mail: ivanlopez@quim.ucm.es; rafael.delgado@salud.madrid.org

J. Katati, C. H. B. da Cruz, P. Mateos-Gil, I. López-Montero
Departamento de Química Física
Facultad de Química
Universidad Complutense
Madrid E-28040, Spain

P. Mateos-Gil, I. López-Montero
Instituto Pluridisciplinar
Paseo Juan XXIII, 1, Madrid 28040, Spain

Therefore, alternative host receptors are also involved in the infection process. Among these receptors, C-type Lectin Receptors (CLRs) as dendritic cell-specific intercellular adhesion molecule-3 grabbing non-integrin (DC-SIGN) and L-SIGN are pathogen recognition receptors identified as mediators of trans-infection and cellular entry.[4] These lectins recognize oligomannose type ligands, which also constitute one third of the N-glycans of SARS-CoV-2 spike.[5] Hence, therapeutics based in the competitive inhibition of virus attachment to DC-SIGN with glycomimetics is a promising anti-infectious strategy. Notably, this host-targeted therapy could plausibly be more resistant to viral adaptative mutations such as those present in SARS-CoV-2 variants like Omicron exhibiting high resistance to the action of neutralizing antibodies.[6]

This strategy has been employed by Bernardi et al. to study the inhibition of SARS-CoV-2 by C-2 triazole modified mannosides as glycomimetics ligands for DC-SIGN.[7] Although these glycomimetics improve over one order of magnitude their affinity in comparison to mannose, the interaction takes place by way of multivalent constructs,[8] and, therefore, more efficient inhibitors are achieved using multivalent glycomimetics.

Multivalent glycomimetics bearing mannose or fucose epitopes have been investigated as inhibitors of DC-SIGN mediated viral infection, as in the case of HIV, Ebola, Zika and Dengue virus infections.[9] Regarding SARS-CoV-2 infection, Fieschi, Delgado et al. found that a previously studied glycomimetic against HIV infection was able to inhibit the interaction of the *S* protein with the lectin receptor and blocked the viral trans-infection of susceptible Vero E6 cells.[4c] Cramer et al. have reported mannosylated poly-L-lysine glycopolymers that efficiently inhibit both SARS-CoV-2 spike binding to DC-SIGN and trans-infection of ACE2+ cells mediated by DC-SIGN in nanomolar concentrations.[10] It is expected, therefore, that multivalent systems able to interact with high affinity with DC-SIGN will also be useful in the treatment of SARS-CoV-2 infections.

In previous works, we have reported glycofullerenes as very effective inhibitors of DC-SIGN mediated infections by Ebola, Zika or Dengue viruses,[11] up to reach picomolar IC_{50} values with a tridecafullerene substituted with 360 α(1,2)mannobioside moieties.[12] Notably, these glycofullerenes pose a biocompatible rigid tridimensional structure that mimics the glycosylated surface of viruses. Moreover, the peripheral carbohydrate shell of glycofullerenes make them water soluble and non-cytotoxic. These carbon nanostructures show a general trend: the higher the number of carbohydrate units, the higher the affinity for DC-SIGN. This tendency was studied from glycofullerenes constituted by only one fullerene unit to oligomers formed by two to four glycofullerenes[13] and tridecafullerenes in which a central C_{60} is covalently bonded to 12 glycofullerenes.[11c,12]

In this work, we have designed new glycofullerene-based structures employing a central porphyrin scaffold.[14] This structural modification is thought to afford a fluorescent rigid molecular framework to conjugate the glycofullerenes. Their inhibitor ability of DC-SIGN as trans-receptor of the infection by SARS-CoV-2 has been evaluated in a trans-infection model and by a cytometric assay that uses transfluorospheres modified by the SARS-CoV-2 spike. Moreover, for that nanostructure showing better inhibition results, its specific interaction with DC-SIGN has been studied through confocal microscopy, NMR binding experiments and QCM experiments, revealing the interaction of glycofullerene with the CRD of the lectin. To get a deeper insight in the carbohydrate-DC-SIGN interaction, we have also carried out *all-atom* molecular dynamics simulations. This computational approach confirms the observation of the glycofullerene interaction with the canonical CRD of DC-SIGN monitored by NMR and QCM experiments.

2. Results and Discussion

2.1. Synthesis and Characterization

The synthetic route to obtain the new multivalent glycoporphyrins 11 and 12 has been performed following a click chemistry strategy.[15] This approach required to design an asymmetric [5:1] hexakis-adduct that bears five alkyne-terminated malonates and one malonate that links a glycofullerene to a central porphyrin core (Scheme S1, Supporting Information).[16] While the former malonate 4 has been previously attached to a C_{60}, the latter is a new linker prepared through the esterification of an asymmetric Br-terminated PEG (1) with ethyl malonyl chloride to obtain 2.[17] Therefore, two sequential Bingel-Hirsch cyclopropanation reactions afforded the asymmetric hexakis-adduct 5 following reported protocols.[11c] Then, glycofullerene 7 was achieved under Copper-catalyzed Azide–Alkyne Cycloaddition (CuAAC) conditions between peripheral alkynes of 5 and the terminal azide of mannose derivative 6. To avoid any interference in the biological assays, 7 was treated with Quadrasil MP to remove any copper traces and the product was precipitated using methanol. The subsequent treatment of 7 with sodium azide under MW radiation and purification through size-exclusion chromatography resulted in the new building block 8, isolated as a brown glassy solid in good yield (see Supporting Information).

Finally, porphyrins 9 and 10 that bear terminal alkyne groups, were clicked with glycofullerene 8 by CuAAC to obtain glycoporphyrins 11 and 12, with yields over 70% (**Figure 1**).[18] To ensure a total functionalization of these porphyrins, a 25% excess of glycofullerene 8 was added. These new compounds (11 and 12) are peripherally decorated with 4 and 8 glycofullerenes, which means 40 and 80 mannose units, respectively.

Both novel intermediates and final compounds were thoroughly characterized by infrared spectroscopy (IR-ATR), ^{1}H and ^{13}C NMR spectroscopy. Although mass spectrometry corroborated the new malonate 2 and monoadduct 3, it was not possible to record the mass spectra for larger structures due to the observed extensive high fragmentation.[12]

R. Delgado
Departamento de Medicina
Facultad de Medicina
Universidad Complutense
Madrid E-28040, Spain

R. Delgado
Instituto de Salud Carlos III
CIBERINFEC
Madrid Spain

N. Martín
Campus de Cantoblanco
IMDEA-Nanoscience
C/ Faraday 9, Madrid 28049, Spain

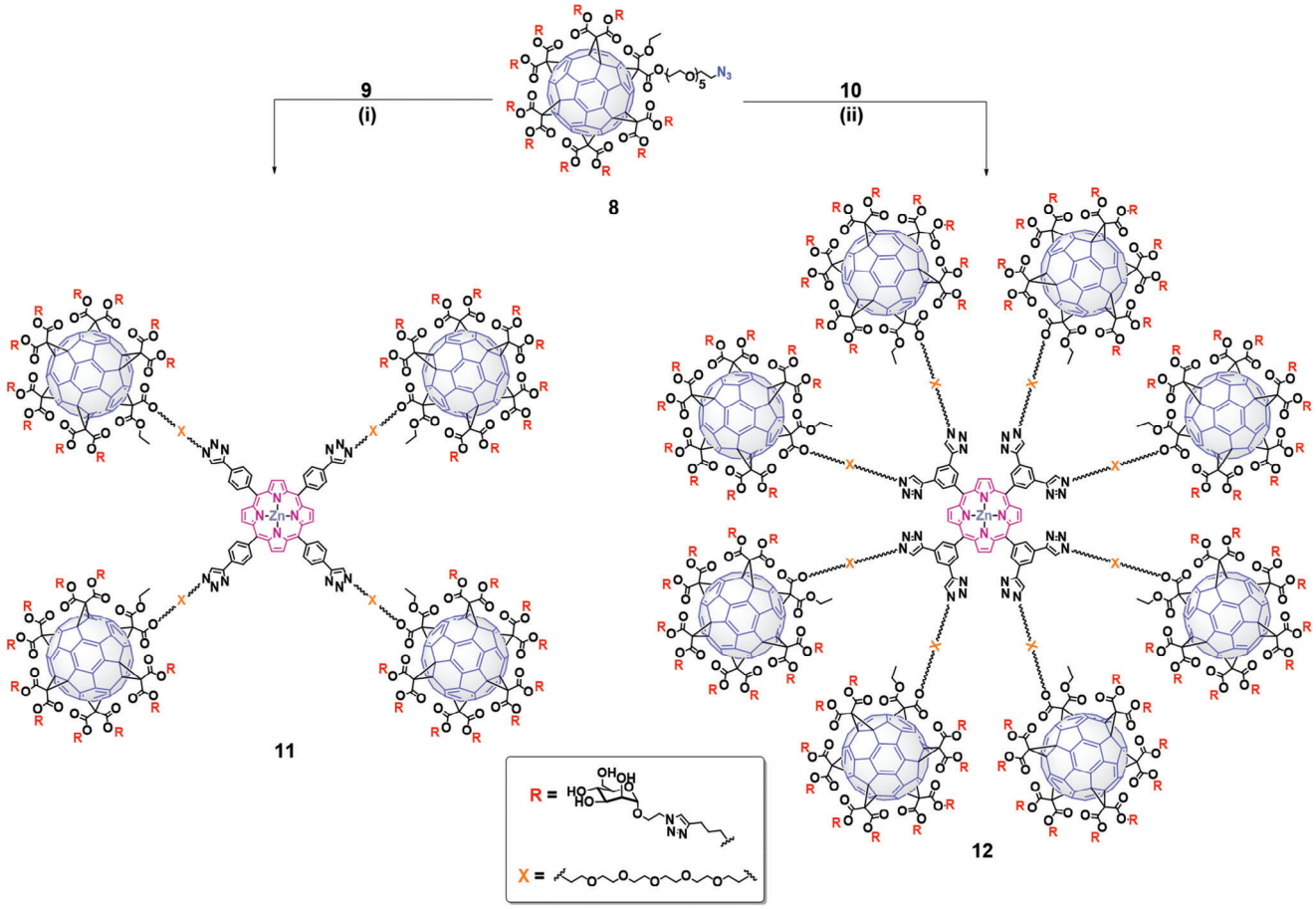

Figure 1. Syntheses of glycoporphyrins 11 and 12 using CuAAC click chemistry. *Reagents and conditions*: i) $CuBr{\cdot}S(CH_3)_2$, sodium ascorbate, Cu^0, DMSO, 72 h (75%); ii) $CuBr{\cdot}S(CH_3)_2$, sodium ascorbate, Cu^0, DMSO, 96 h (74%).

Because of the asymmetric substitution geometry of [60]fullerene monoadducts, ^{13}C NMR peaks are usually difficult to assign. Most fortunately, however, is the assignment by ^{13}C NMR of molecules bearing C_{60} hexakis-adducts, as their high symmetry (T_h) provides simpler resonance distribution patterns. Therefore, obtaining hexakis-adduct 5 from monoadduct 3 results in a reduction of fullerene C_{sp^2} resonances from fifteen to the typical two signals *circa* 141 and 145 ppm (Figures S6 and S10, Supporting Information). Then, the successful functionalization of 7 with mannose could also be confirmed by ^{13}C NMR upon the disappearance of the alkynyl resonances (*C*≡*C*H) of 5, and the rising of new peaks from the triazole rings at ≈146 and 123 ppm (Figure S13, Supporting Information). Additionally, triazole C—H protons are easily identified by ^1H NMR as a broad singlet near 8 ppm (Figure S12, Supporting Information). As the last synthetic step to get 8 involves the replacement of a bromine atom by an azido group, FTIR was useful due to the appearance of the azido band at υ = 2108 cm^{-1} (Figure S17, Supporting Information). Moreover, ^{13}C NMR unequivocally shows the disappearance of the *C*—Br signal at ≈32 ppm and the appearance of a new resonance at ≈50 ppm attributed to the *C*—N_3 (Figure S16, Supporting Information).

For the target glycoporphyrins 11 and 12, ^1H NMR spectra show broadened signals ascribed to probable intermolecular aggregation, as observed in other carbohydrate-rich nanostructures.[12] However, it is still possible to detect resonances corresponding to each porphyrin core (β-H and H_{Ar}) between 8.5 and 9.0 ppm, the triazole C—H signals ≈8 ppm, as well as broad carbohydrate and PEG resonances displayed in the range from 3.0 to 4.8 ppm (Figures S18 and S23, Supporting Information). Again, ^{13}C NMR provides straightforward evidence of the structure of final glycoconjugates (**Figure 2**). The disappearance of terminal alkyne resonances ≈75–85 ppm confirms the complete peripheral functionalization (Figures S19 and S24, Supporting Information). Additionally, the resonances from C_{sp^2} of [60]fullerene are easily identified near 141 and 145 ppm. This, together with the disappearance of the *C*—N_3 signal ≈50 ppm, indicates that click reactions were successfully conducted. 2D NMR experiments were also carried out to confirm the proposed structures (Figures S20 and S25, Supporting Information). Moreover, through FTIR analysis, the azido group band from 8 is not detected (Figures S21 and S26, Supporting Information).

The characterization of these nanostructures was completed with steady-state absorption spectra recorded in water solutions (10^{-6} M) (Figures S22 and S27). UV–vis experiments confirm the presence of both light-active moieties, i.e., peripheral C_{60} hexaadducts and porphyrin cores. A broad high-energy absorption

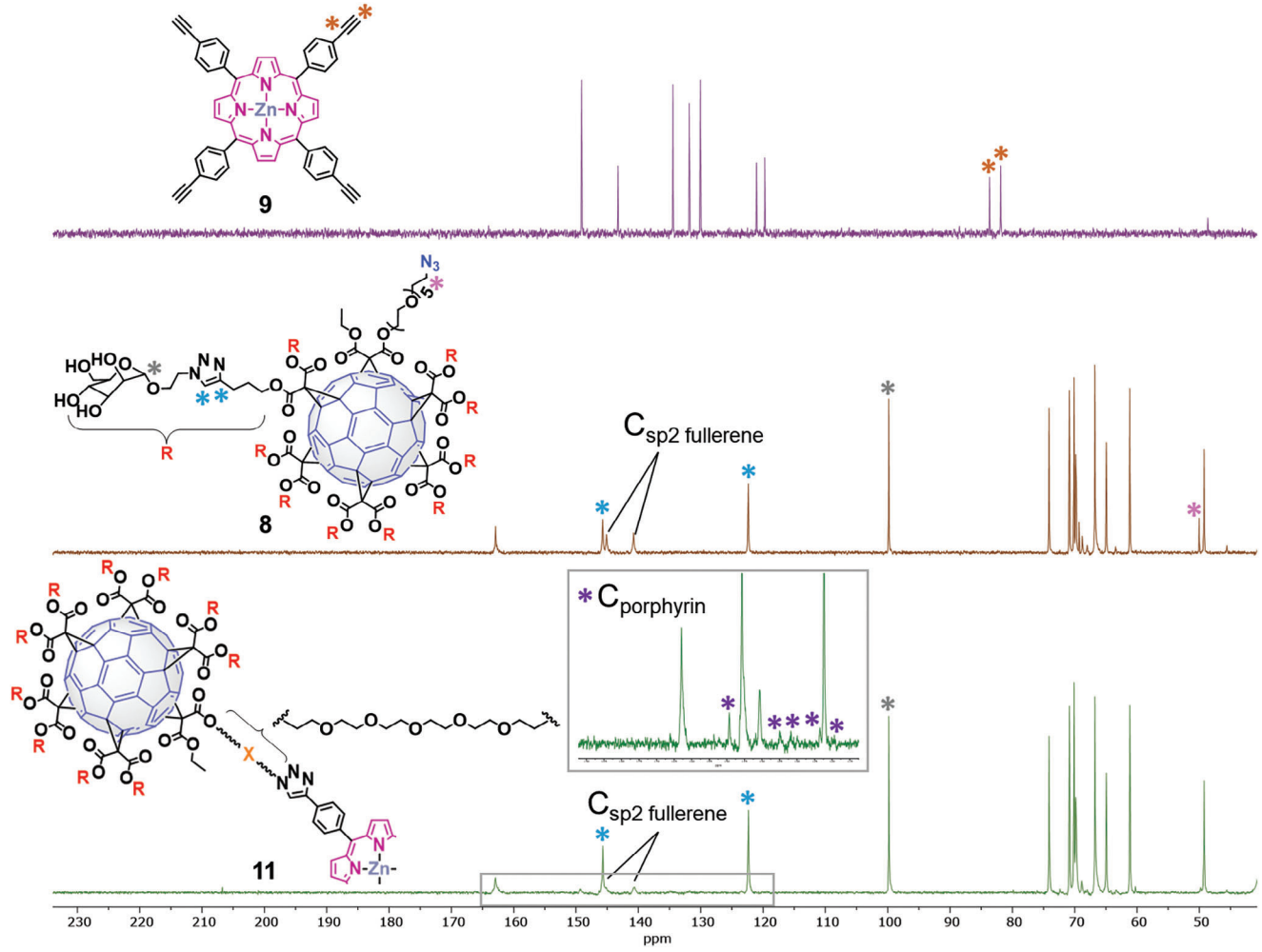

Figure 2. Partial view of the ^{13}C NMR spectra (DMSO-d_6, 176 MHz). Compounds 8 (middle), 9 (up) and 11 (down).

band found at $\lambda < 400$ nm is attributed to glycofullerenes and the strong absorption at $\lambda \approx 436$ nm and a series of bands at $\lambda \approx 564$ and 607 nm correspond to the well-known Soret band and Q-bands from porphyrins.[19] The emission properties in water show the two common fluorescence peaks from the porphyrin-core (Figure S28, Supporting Information), the higher energy band at 607–614 nm and the lower one in the range of 661–667 nm.[14a]

DOSY (Diffusion-Ordered NMR SpectroscopY) NMR experiments (≈2 mg mL in D_2O, Figures S29,S30, and S31, Supporting Information) have been used to get an estimation of the overall molecular size of the glycoporphyrins 11 and 12.[20] This technique allows obtaining the diffusion coefficient (D) and the estimation of the hydrodynamic radius (R_H) according to the Stokes–Einstein equation, assuming a spherical shape.[21] Molecular weights (MW), D and R_H values are shown in **Table 1**. Additionally, D was determined for a previously described symmetric hexakis-adduct glycofullerene (Hexa-MAN, Figure S36, Supporting Information)[11a] to compare with 11 and 12. Then Hexa-MAN that contains only one central fullerene shows R_H of 11.4 Å, in agreement with the result obtained by ^1H NMR pulsed-field-gradient (PFG) diffusion experiments.[22] As expected, when glycofullerenes are arranged around the porphyrin core, 11 and 12 display a considerable increase in the overall size with R_H of 22.9 and 45.6 Å, respectively. These results show a remarkable correlation between D and MW, which is also an indication of the correct functionalization of the starting porphyrins with glycofullerene 8.

Table 1. Diffusion coefficients determined by DOSY and hydrodynamic radii.

Compound	Molecular Weight (MW)	Diffusion coefficient (D, $m^2\ s^{-1}$)	Hydrodynamic radii (R_H, Å)
Hexa-MAN	5116.77	$2.14 \cdot 10^{-10}$	11.4
11	19 988.94	$1.07 \cdot 10^{-10}$	22.9
12	39 298.37	$5.37 \cdot 10^{-11}$	45.6

In order to complete the characterization of these nanostructures, DLS and Transmission Electron Microscopy (TEM) experiments were conducted. DLS analysis (H_2O, $1 \cdot 10^{-5}$ M) show two or three main distributions for 11–12 (Figures S32 and S33, Supporting Information), which is compatible with a

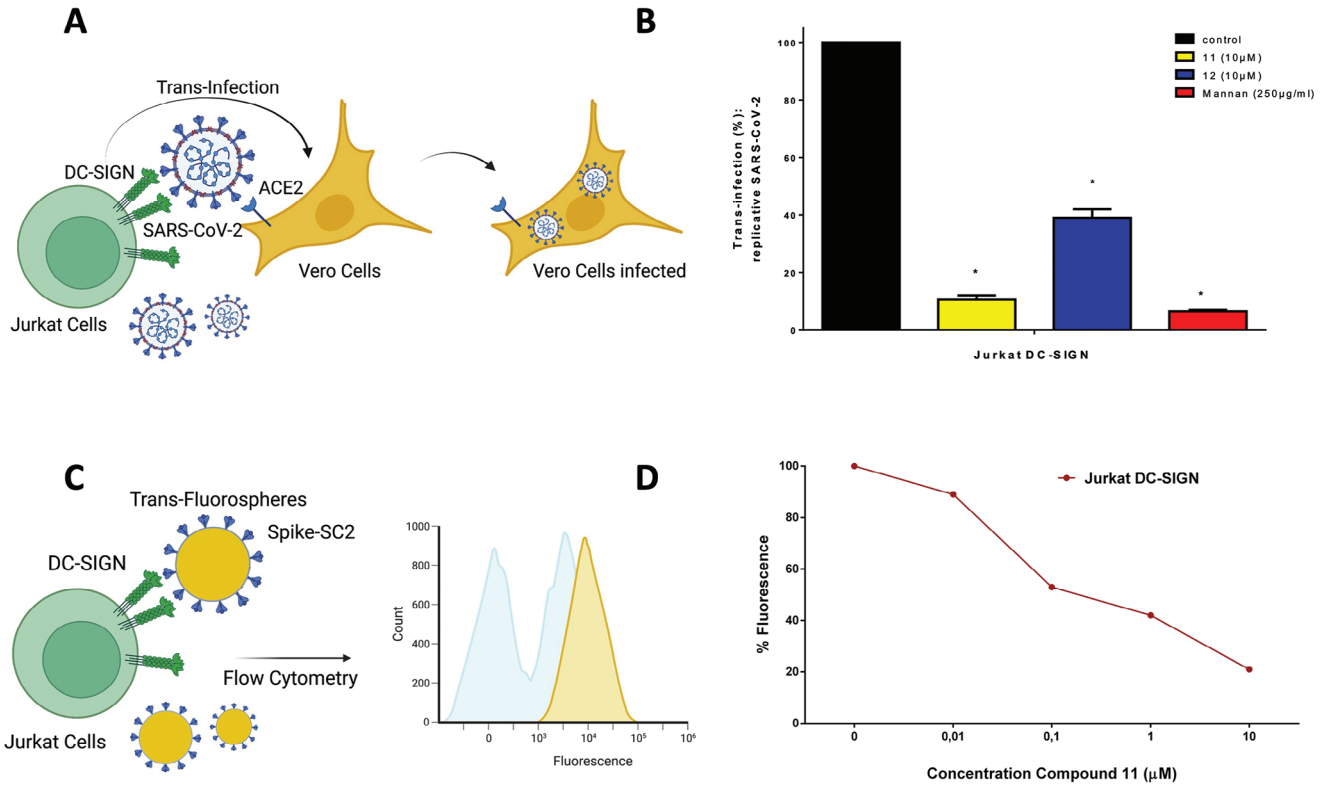

Figure 3. A) Scheme of the trans-infection mechanisms in which lectins (DC-SIGN) on the cellular surface bind to the S protein of SARS-CoV-2 thus facilitating the infection of susceptible (ACE2+) cells; B) Trans-infection of authentic SARS-CoV-2 (Wu-hu-1 S-D614G) in the presence or not (control) of 1 μM of compound 11 or 12. Results are expressed as % of the trans-infection control. *** p <0.01; C) Scheme of the binding experiment with trans-fluorospheres coated with SARS-CoV-2 S protein and DC-SIGN-expressing Jurkat cells; D) Binding between SARS-CoV-2 S-coated transfluorospheres and DC-SIGN-expressing Jurkat cells in the presence or not (control) of increasing amounts of compound 11, was measured by flow cell cytometry. Results are expressed as % of fluorescence as compared with the no compound control test.

weakly cooperative aggregation in H_2O. The first size encountered (≈9 nm) must correspond to one molecule, while the rest arise from the aggregation of several molecules. TEM images of 11 and 12 (Figures S34 and S35, Supporting Information) reveal the presence of the smallest size distribution of spherical particles ≈9 nm, which correspond to a few or even just one molecule. These results agree with the smaller size distribution found in DLS and are also in the range of the R_H described above.

2.2. Biological Assays

C-Type lectin receptors such as DC-SIGN bind to glycan motifs expressed at the envelope glycoproteins of viruses such as SARS-CoV-2 and promote trans-infection of ACE2 expressing cells. We tested porphyrins 11 and 12 as inhibitors of DC-SIGN binding to SARS-CoV-2 spike using authentic SARS-CoV-2 in a trans-infection model. This was completed with a flow cell cytometry assay using transfluorospheres conjugated with SARS-CoV-2 S-protein (**Figure** 3a,c).

During trans-infection, viral particles bind to lectins that are located on the cell membrane and after extensive washes to remove virus not attached to the cells, these particles are later efficiently transferred to susceptible cells (Figure 3A). Trans-infection assays have been carried out with cells that express DC-SIGN on their surface, since it has already been described that this receptor is capable of recognizing the glycosylated structures of the SARS-CoV-2 S protein.[4c,7,23]

Jurkat cells are a T-lymphocyte cell line and do not express ACE2 in their membrane, therefore, the DC-SIGN lectin would be the only surface molecule capable of interacting with the SARS-CoV-2 glycoprotein, establishing a bond through S-glycosylations.

Before evaluating the antiviral activity of these compounds, cytotoxicity tests for 11 and 12 were performed (Figure S37, Supporting Information). Initial results show cell toxicity starting from a concentration of 10 μM. Therefore, the following trans-infection assays were performed using compound concentrations that do not alter cell viability, that is 1 μM.

For SARS-CoV-2 it was observed the inhibitory capacity for compounds 11 and 12 in cells that express DC-SIGN in trans-infection experiments (Figure 3B): 89.5 and 61% inhibition of trans-infection respectively. Since compound 11 exhibited better inhibition for SARS-CoV-2 virus on Jurkat-DC-SIGN (although not statistically significant), additional studies were carried for this nanostructure.

In this case, flow cytometry was a useful technique to complete the inhibitory activity of 11. This study provides information about interaction between DC-SIGN lectins and SARS-CoV-2

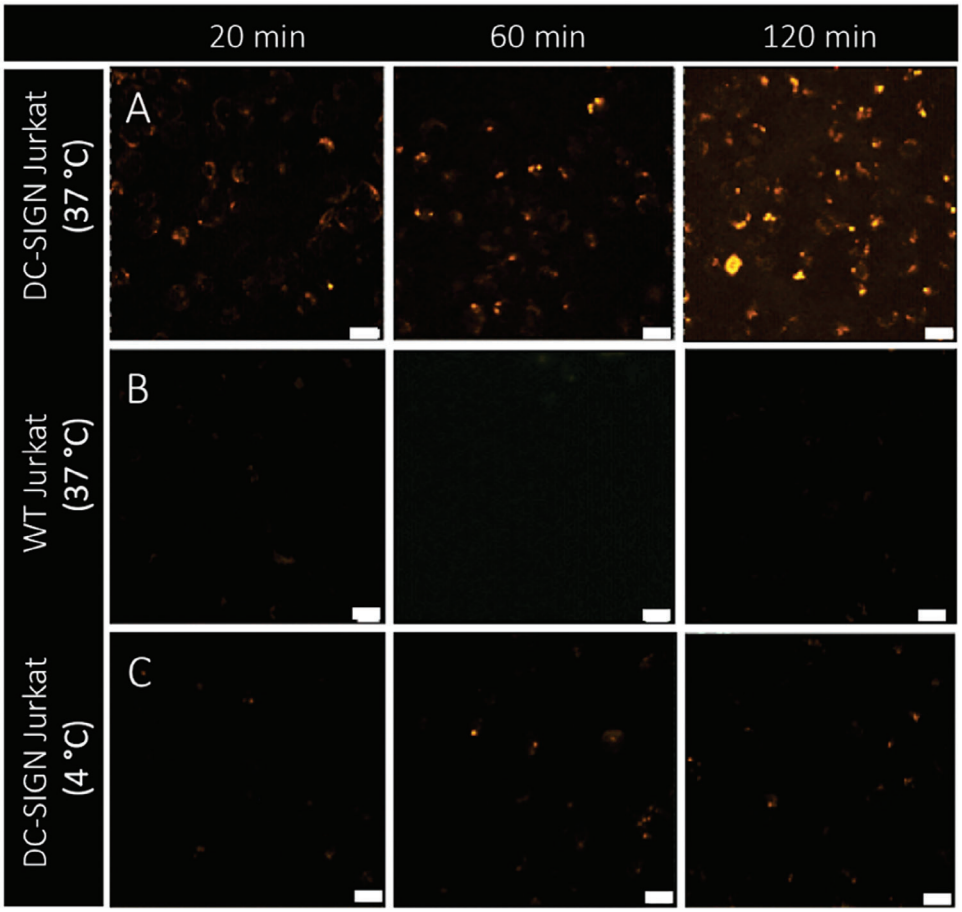

Figure 4. Confocal fluorescence micrographs of Jurkat cells incubated with 1 μM of glycoporphyrin 11. A) DC-SIGN-expressing Jurkat cells at 37 °C. Glycoporphyrin 11 internalizes and reaches the inner environment of cells through endosomal trafficking; B) WT Jurkat cells at 37 °C; C) DC-SIGN-expressing Jurkat cells at 4 °C. Note that glycoporphyrin 11 does not stain the cytosolic environment of the cell in B) and C). λ_{exc} = 561 nm, λ_{em} >561 nm. See main text for details. Scale bars are 10 μm.

S-protein in the absence (control) and upon addition of 11. To monitor this interaction, flow cell cytometry detects fluorescence emission arising from fluorescent beads (transfluorospheres) conjugated with the soluble trimeric and pre-fusion stabilized SARS-CoV-2 S-protein (Figure 3C). As shown in Figure 3D, addition of compound 11 on Jurkat-DC-SIGN cells gradually reduces the fluorescence signal percentage down to 40% at 1 μM and 20% at 10 μM (it should be noted that the 10 μM concentration was toxic for cells as shown in Figure S37, Supporting Information).

Both trans-infection and binding experiments coincide in pointing out the specificity of porphyrin 11 as a good inhibitor of the interaction of SARS-CoV-2 with the DC-SIGN lectin.

2.3. Selective Uptake of Glycoporphyrin 11 by DC-SIGN-Mediated Endocytosis

To first assess the specific interaction of glycoporphyrin 11 with the DC-SIGN lectin we took advantage of its uptake in cultured Jurkat cells. The fluorescence emission of the porphyrin core was used to trace glycoporphyrins inside cells by means of confocal fluorescence microscopy (**Figure 4**). Based on the cell viability experiments (Figure S38, Supporting Information), WT Jurkat cells and DC-SIGN-expressing Jurkat cells were incubated with glycoporphyrin 11 at 1 μM concentration to avoid cytotoxicity. To better characterize a receptor-mediated endocytosis typical for the internalization of macromolecules, cells were imaged up to 2 h (early uptake) to minimize the non-specific endocytosis occurring at longer times. When DC-SIGN-Jurkat cells were incubated at 37 °C with glycoporphyrin 11, an increasing red fluorescence signal was observed at the surface membrane and within the intracellular environment upon internalization (Figure 4A). Unlike DC-SIGN-expressing Jurkat cells, WT Jurkat cells showed a very dim background when incubated at 37 °C with glycoporphyrin 11 at similar concentration and times and imaged with the same acquisition settings (Figure 4B). As temperature is a critical factor that impacts severely in endocytosis, additional experiments were run at 4 °C. At this temperature, endocytosis is negligible, and no labeling of intracellular media could be imaged but the fluorescence intensity was found at the rim of cells (Figure 4C). These observations suggest a selective uptake of glycoporphyrin 11, whereby the macromolecule first binds to the lectin surface receptor through carbohydrate–protein interactions.

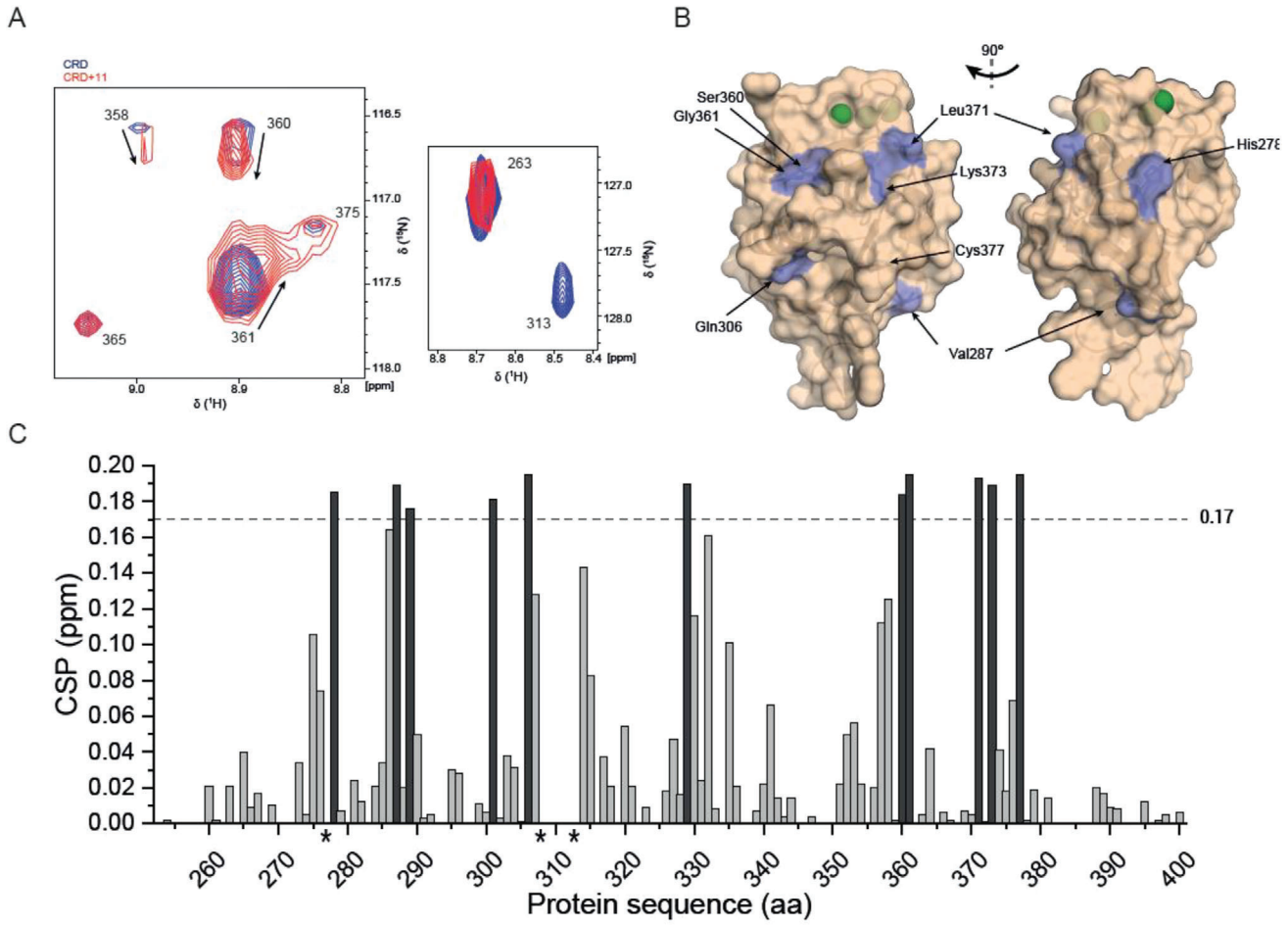

Figure 5. A) Expansion of the ^{1}H-^{15}N HSQC spectra of DC-SIGN CRD in the absence (blue color) and in the presence (red color) of glycoporphyrin 11 (the spectra are overlaid); B) Representation of the crystal structure of DC-SIGN CRD (PDB ID:7NL7) with the residues with the highest perturbation upon addition of compound 11; C) Chemical shift perturbation for each residue; signals that disappear in the presence of glycoporphyrin 11 are marked with an asterisk.

2.4. NMR Binding Experiments

Binding of the glycoporphyrin 11 to the carbohydrate recognition domain (CRD) of DC-SIGN was monitored by ^{1}H–^{15}N Heteronuclear Single Quantum Coherence (HSQC) experiments (**Figure 5**). ^{15}N labelled protein was overexpressed in *E. coli BL21 (DE3)*, solubilized from inclusion bodies and refolded as described in methods section. HSQC resonances were identified based on reported assignments (BMRB code 27 854).[24]

Addition of glycoporphyrin 11 to DC-SIGN CRD (1:4 molar ratio) induced line broadening of the protein signals. This effect is due to the presence of dynamic processes in the intermediate exchange regime in the NMR chemical shift time scale, thus pointing out that the molecules interact. Signals of W277, S308 and F313 disappear upon addition of glycoporphyrin 11. In addition, chemical shift perturbations were detected for certain residues. The more affected NHs are S360, G361, L371, K373, C377, H278, V287, N301, Q306, and S307. These residues are located in regions that also experiment changes in previously reported NMR titrations of DC-SIGN with Lewis^{x} and mannose, confirming that the glycoporphyrin 11 interacts with the canonical carbohydrate binding site.[24b,25]

2.5. Acoustic Measurements of the Interaction Between Glycoporphyrin 11 and CRD

We also studied the interaction between glycoporphyrin 11 and DC-SIGN carbohydrate recognition domain (CRD) using a surface acoustic sensor combined with a membrane model system. We employed a quartz crystal microbalance (QCM) to follow in real-time the formation of a supported lipid bilayer (SLB) and the attachment of CRD His-tagged construct by means of NTA lipid linker (**Figure 6A**). Then, we registered the binding of glycoporphyrin 11 to the membrane-bound CRD protein. Figure 6B shows a representative QCM sensogram depicting changes in the resonant frequency (ΔF) of a crystal sensor during a typical experiment. Initially, the formation of a lipid bilayer was confirmed by the transient presence of a minimum frequency and a final frequency change due to the bilayer formation $\Delta F_{SLB} \approx -200$ Hz

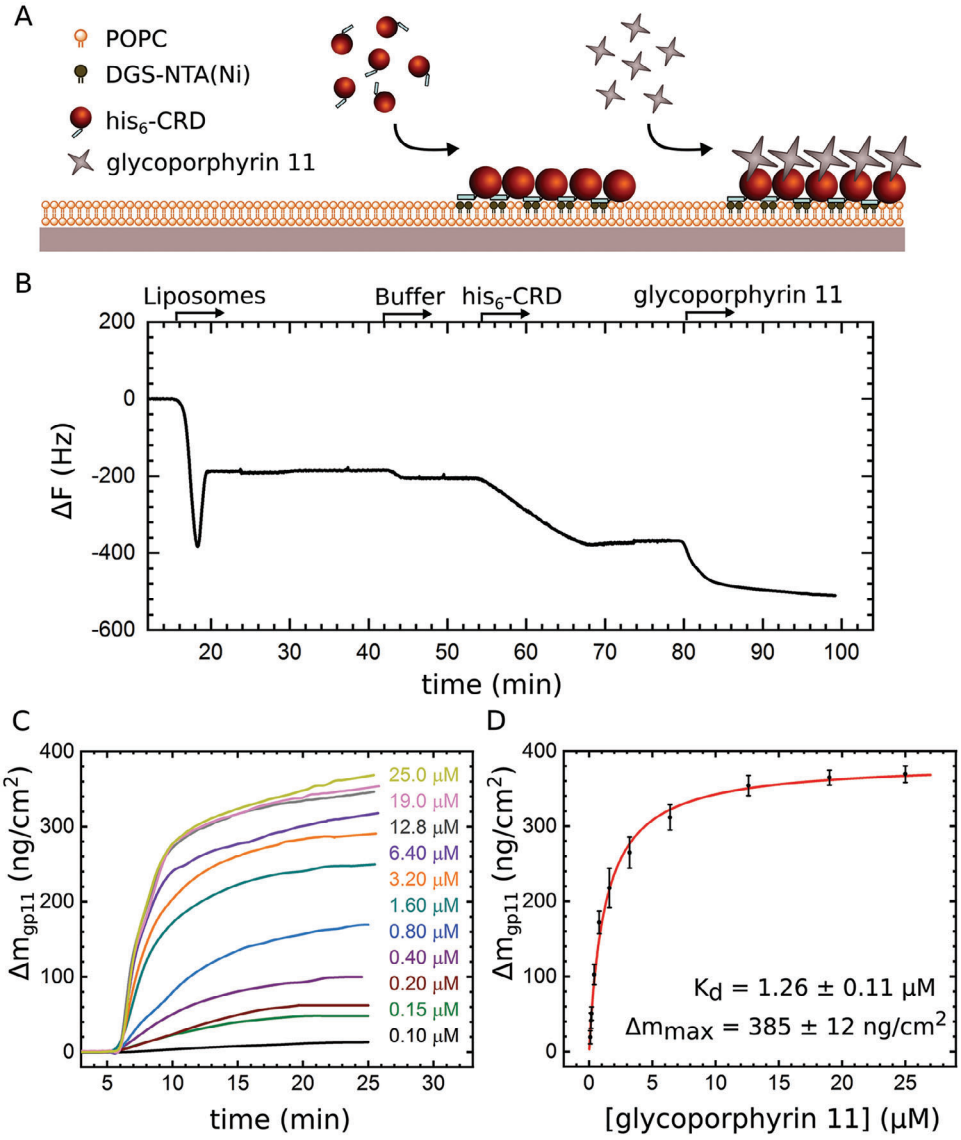

Figure 6. Interaction between glycoporphyrin 11 and his-tagged DC-SIGN carbohydrate recognition domain (his-CRD) oriented on supported lipid bilayers. A) Cartoon showing sequential reconstitution of his_6-CRD onto a lipid bilayer containing NTA lipids followed by glycoporphyrin 11 binding. B) Acoustic sensogram depicting registered changes in the resonant frequency of a silica crystal sensor (ΔF) upon consecutive injections of: 1) liposomes; 2) exchange between liposome adsorption buffer and CRD protein buffer; 3) 1.5 μM solution of CRD his-tagged construct; and 4) glycoporphyrin 11 solutions at 25 μM. C) Sensograms depicting changes in surface-bound mass Δm_{gp11} upon injection of glycoporphyrin 11 at increasing concentrations between 0.1 and 25 μM. D) Average values of Δm_{gp11} obtained from two independent experiments (measured at t = 25 min) versus the concentration of glycoporphyrin 11 in the bulk. Binding dissociation constant K_d describing the interaction between glycoporphyrin 11 and CRD was obtained fitting the experimental data to Langmuir isotherm (red line) see material and methods for details.

as described previously.[26] Subsequently, a small frequency shift was observed due to differences in density and viscosity upon exchange between liposome adsorption buffer and CRD protein buffer. In a second stage, injection of ~ 350 μL of 1.5 μM CRD protein solution led to a frequency change ΔF_{CRD} ≈−155 Hz corresponding to a surface density Δm_{CRD} ≈403 ng cm^{-2} or 20.5 pmol cm^{-2} (i.e., the amount of membrane-bound CRD corresponds to a high surface coverage with a projected area per molecule of ≈8.6 nm^2, in other words 1 molecule occupies in average a circle of ~ 1.6 nm radius).[27] The absence of binding to bilayers lacking NTA lipids and the complete elution upon of the surface attached protein by 200 mM imidazole confirmed the specificity of the binding (Figure S38, Supporting Information). Finally, the binding of glycoporphyrin 11 was monitored and the registered frequency shift ΔF_{gp11} was transformed into surface density Δm_{gp11}. Figure 6C shows sensograms corresponding to injections of increasing concentrations of glycoporphyrin 11 between 0.1 and 25 μM. Values of Δm_{11} where directly calculated from ΔF_{gp11} subtracting the frequency change due to changes in solution viscosity because of the presence of DMSO. The experimental Δm_{gp11} as a function of the concentration of glycoporphyrin 11 (Figure 6D) could be fitted to a Langmuir isotherm. The

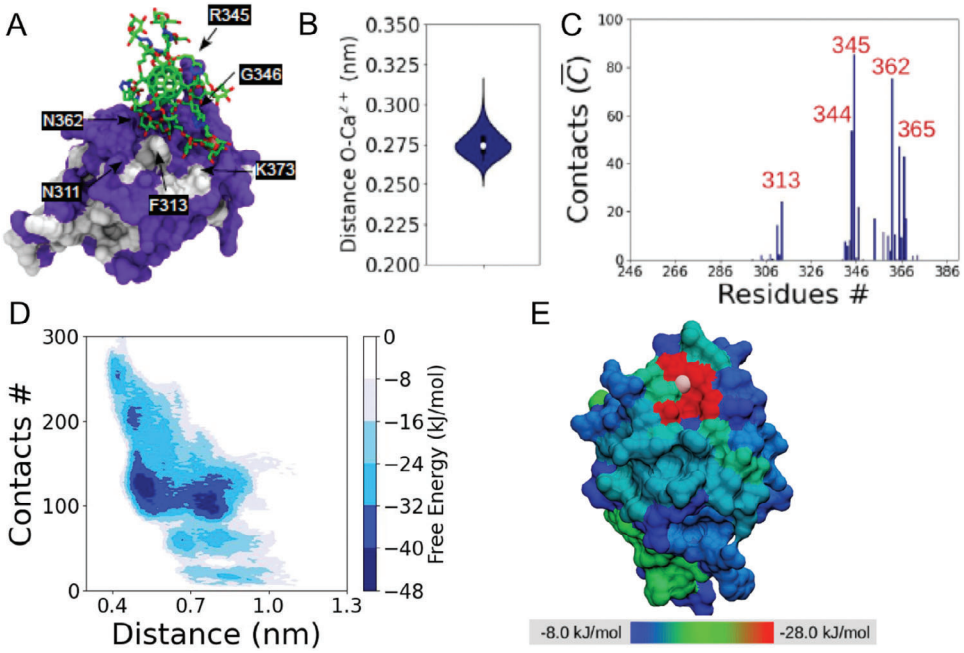

Figure 7. A) Structure of Hexa-MAN complexed to CRD protein. Hexa-MAN is represented in licorice, with carbon, oxygen, and nitrogen atoms in green, blue and red, respectively. The surface of the protein is shown with polar and non-polar residues denoted by violet and white colors. Ca^{2+} is shown in pink. Amino acids in contact with Hexa-MAN are shown. B) Minimum distance between Hexa-MAN oxygens and the Ca^{2+} atom. C) Number of total contacts at Hexa-MAN – CRD interface within 0.4 nm cutoff. D) Binding free energy contour map as defined by metadynamics. E) Front view of the CRD protein surface. The color scale displays the mannose binding free energy on CRD amino acids provided by molecular docking assays. Ca^{2+} is shown in pink.

obtained values for the dissociation constant of the interaction between glycoporphyrin 11 and CRD and the binding saturation were $K_d \approx 1.26 \pm 0.11$ μM and $\Delta m_{max} \approx 385 \pm 12$ ng cm^{-2}, respectively. As expected, the latter value is in good agreement to a 1:1 stoichiometry for the glycoporphyrin 11:CRD interaction at saturation and corresponds to a mean molecular area of 8.9 nm^2, with an estimated radius of 1.7 nm, which agrees with the obtained value from Diffusion NMR experiments (Table 1). Interestingly, the low K_d value obtained here suggests that inhibitory effect of glycoporphyrin 11 is based on the competition with SARS-CoV-2 spike for DC-SIGN binding, which is characterized by a larger K_d ≈5–10 μM.[4c]

2.6. Molecular Dynamics Simulations

To further evaluate the carbohydrate-DC-SIGN interaction we ran *all-atom* molecular dynamic simulations. For simplicity, and because we focused on the carbohydrate-protein interaction, only one symmetric C_{60}-hexakis-adduct of the glycoporphyrin 11 (Hexa-MAN) and the CRD of DC-SIGN were simulated (**Figure** 7A; Video S1, Supporting Information). An important validation criterion in the modeling of the inhibitory effect of glycoporphyrin 11 relies on the Ca^{2+} coordination to hydroxyl groups of carbohydrates; a binding signature widely reported in the literature and strengthened by crystallographic data.[27] After computing the minimum distance between Ca^{2+} and oxygen from mannoses (O) (Figure 7B), one replica was able to maintain a minimum O-Ca^{2+} distance of 0.26 nm, similar to the O-Ca^{2+} bond length observed in the crystallographic results (0.27 nm).[27] As in case of NMR experiments, additional binding contacts (within 1.0 nm cutoff radius) between mannoses and amino acid side chains were observed. In particular, F313, R345, S360, G361, N362 and K373 were explored by the flexible imidazole-based linkers (Figure 7C). The basic or acid nature of R345, N362 and K373 provides an extensive polar area around Ca^{2+} for mannose interaction through hydrogen bond formation (Figure 7A).

To get deeper insight into the thermodynamic contribution of both mannose-Ca^{2+} and mannose-residue interactions we computed the unbound free energy landscape (Figure 7D). The binding free energy maps displayed two well-defined energy wells of −48 kJ mol^{-1} that occur at two different stages upon detachment, i.e., with increasing distance. The time trajectory showed strong and persistent interactions at Q304, E358, S360, G361, and N362 and the dominant interaction governed by the Ca^{2+} binding site. In addition to the dominant Ca^{2+} coordination to mannoses, these observations introduce cooperative and auxiliary interactions of mannoses with the CRD. Based on this observation, we screened for single mannose binding sites on the whole CRD surface (Figure 7E). As expected, the highest affinity was identified around the canonical binding site (stained in red), followed by the surrounding amino acids (stained in green). This result is in agreement with the NMR analysis, since the most affected aminoacids upon addition of glycoporphyrin 11 are located around the canonical binding site.

3. Conclusion

Multivalent porphyrin-cored 11 and 12, bearing 4, and 8 glycofullerenes respectively, have been prepared by following a straightforward and highly efficient multistep synthetic procedure. The new compounds have been thoroughly characterized through FTIR spectroscopy, ^{1}H, ^{13}C and DOSY NMR measurements and the hydrodynamic radii (R_H) were calculated. The new glycoporphyrins show water solubility due to the peripheral 40 or 80 mannose residues and display fluorescence emission, that arise from the central porphyrin scaffold. This allowed in vitro confocal microscopy studies, which is as a straightforward technique to prove that these macromolecules are efficiently attached and internalized through Jurkat cells membrane when DC-SIGN is present.

The role of alternative cellular receptors for SARS-CoV-2 in COVID-19 pathogenesis is subjected to intensive research and lectins such as DC-SIGN have been demonstrated to participate in the infection process being potentially a target for antibody neutralization and antiviral strategies. In this respect, here we show that blocking the specific interaction of DC-SIGN with SARS-CoV-2 through the interaction with the highly glycosylated S protein can be achievable with synthetic glycofullerenes. We have used two methodologies to explore this inhibition: a well stablished infection assay with authentic SARS-CoV-2 S protein and a binding assay with fluorescent transfluorospheres coated also with the viral S protein. Glycoconjugate 11 showed a clear inhibitory effect in blocking DC-SIGN-mediated SARS-CoV-2 trans-infection since it could almost (89.5%) abolish Jurkat-DC-SIGN SARS-CoV-2 transfer to susceptible cells. This was also correlated in the binding assay in which compound 11 exhibited a clear dose response inhibition of binding of DC-SIGN and S protein. This is an interesting proof of concept of the potential application of this strategy with antiviral purposes. Interestingly, even though glycoconjugate 12 possesses double mannose units than 11, the later showed a better performance in DC-SIGN mediated trans-infection of SARS-CoV-2 what suggests a high specificity of the blocking mechanism.

Although further research is warranted to explore and define the optimal molecular basis of this valuable antiviral strategy, specific interaction of glyconjugate 11 with DC-SIGN receptor was confirmed by ^{1}H-^{15}N HSQC NMR experiments. For this purpose, DC-SIGN carbohydrate recognition domain was overexpressed in *E. coli* labelled with ^{15}N. Addition of 11 to DC-SIGN CRD induced perturbation of the protein signals pointing out that 11 binds to the protein. The analysis of the protein NH perturbations allows defining the interaction area that is located around the calcium ion in the canonical binding site described for mannose and Lewis^{x} saccharides.

The binding affinity of 11 to the DC-SIGN carbohydrate recognition domain was characterized by a 1:1 stoichiometry and a K_d ≈1.26 ± 0.11 μM as measured by acoustic measurements using a QCM. This value is one order of magnitude lower than the binding constant of SARS-CoV-2 spike to DC-SIGN reported in the literature. The high affinity of 11 to DC-SIGN suggests that the trans-infection inhibitory effect of these compounds is likely operated through a competitive mechanism where the mannoses from 11 directly interact with the carbohydrate-binding site of DC-SIGN as visualized by molecular dynamics simulations.

Supporting Information

Supporting Information is available from the Wiley Online Library or from the author.

Acknowledgements

This work was partially supported by the European Union (ANTICIPA-UCM PR38/21-22), Comunidad de Madrid (PR65/19-22339) and Spanish Agencia Estatal de Investigación (PID2020-115120GB-I00 and PID2019-105237GB-I00). The authors thanks the National Laboratory for Scientific Computing (LNCC/MCTI, Brazil) by the HPC resources of the Santos Dumont supercomputer (ID #45691, project "virusevolution"). J.C.-G. thanks the Comunidad de Madrid Atracción de Talento Program (2018-T2/BMD-10275). The authors thank the Nuclear Magnetic Resonance facilitites from Universidad Complutense.

Conflict of Interest

The authors declare no conflict of interest.

Data Availability Statement

The data that support the findings of this study are available in the supplementary material of this article.

Received: November 20, 2023
Published online:

[1] WHO. Coronavirus (COVID-19) Dashboard, https://covid19.who.int/ (accessed: February **2023**).
[2] a) L. Samavati, B. D. Uhal, *Front. Cell. Infect. Microbiol.* **2020**, *10*, 317; b) M. Hoffmann, H. Kleine-Weber, S. Schroeder, N. Krüger, T. Herrler, S. Erichsen, T. S. Schiergens, G. Herrler, N.-H. Wu, A. Nitsche, M. A. Müller, C. Drosten, S. Pöhlmann, *Cell* **2020**, *181*, P271; c) M. Khodadoost, Z. Niknam, M. Farahani, M. Razzaghi, M. Norouzinia, *Gastroenterol. Hepatol. Bed Bench.* **2020**, *13*, 374.
[3] a) S. M. Christie, T. Tada, Y. Yin, A. Bhardwaj, N. R. Landau, E. Rothenberg, *Sci. Adv.* **2022**, *8*, eabo3977; b) J. Liu, F. Lu, Y. Chen, E. Plow, J. Qin, *J. Biol. Chem.* **2022**, *298*, 101710.
[4] a) F. A. Lempp, L. B. Soriaga, M. Montiel-Ruiz, F. Benigni, J. Noack, Y.-J. Park, S. Bianchi, A. C. Walls, J. E. Bowen, J. Zhou, H. Kaiser, A. Joshi, M. Agostini, M. Meury, E. Dellota, S. Jaconi, E. Cameroni, J. Martinez-Picado, J. Vergara-Alert, N. Izquierdo-Useros, H. W. Virgin, A. Lanzavecchia, D. Veesler, L. A. Purcell, A. Telenti, D. Corti, *Nature* **2021**, *598*, 342; b) R. Amraei, W. Yin, M. A. Napoleon, E. L. Suder, J. Berrigan, Q. Zhao, J. Olejnik, K. B. Chandler, C. Xia, J. Feldman, B. M. Hauser, T. M. Caradonna, A. G. Schmidt, S. Gummuluru, E. Mühlberger, V. Chitalia, C. E. Costello, N. Rahimi, *ACS Cent. Sci.* **2021**, *7*, 1156; c) M. Thépaut, J. Luczkowiak, C. Vivès, N. Labiod, I. Bally, F. Lasala, Y. Grimoire, D. Fenel, S. Sattin, N. Thielens, G. Schoehn, A. Bernardi, R. Delgado, F. Fieschi, *PLoS Pathog.* **2021**, *17*, e1009576.
[5] Y. Watanabe, J. D. Allen, D. Wrapp, J. S. Mclellan, M. Crispin, *Science* **2020**, *369*, 330.
[6] Q. Wang, S. Iketani, Z. Li, L. Liu, Y. Guo, Y. Huang, A. D. Bowen, M. Liu, M. Wang, J. Yu, R. Valdez, A. S. Lauring, Z. Sheng, H. H. Wang, A. Gordon, L. Liu, D. D. Ho, *Cell* **2023**, *186*, P279.
[7] S. Pollastri, C. Delaunay, M. Thépaut, F. Fieschi, A. Bernardi, *Chem. Commun.* **2022**, *58*, 5136.
[8] D. Budhadev, E. Poole, I. Nehlmeier, Y. Liu, J. Hooper, E. Kalverda, U. S. Akshath, N. Hondow, W. B. Turnbull, S. Pöhlmann, Y. Guo, D. Zhou, *J. Am. Chem. Soc.* **2020**, *142*, 18022.

[9] a) Y. Van Kooyk, T. B. H. Geijtenbeek, *Nat. Rev. Immunol.* **2003**, *3*, 697; b) N. Rahimi, *Biology* **2021**, *10*, https://doi.org/10.3390/biology10010001; c) C. P. Alvarez, F. T. Lasala, J. Carrillo, O. Muñiz, A. L. Corbi, R. Delgado, *J. Virol.* **2002**, *76*, 6841.

[10] a) J. Cramer, B. Aliu, X. Jiang, T. Sharpe, L. Pang, A. Hadorn, S. Rabbani, B. Ernst, *ChemMedChem* **2021**, *16*, 2345; b) J. Cramer, A. Lakkaichi, B. Aliu, R. P. Jakob, S. Klein, I. Cattaneo, X. Jiang, S. Rabbani, O. Schwardt, G. Zimmer, M. Ciancaglini, T. Abreu Mota, T. Maier, B. Ernst, *J. Am. Chem. Soc.* **2021**, *143*, 17465.

[11] a) J.-F. Nierengarten, J. Iehl, V. Oerthel, M. Holler, B. M. Illescas, A. Muñoz, N. Martín, J. Rojo, M. Sánchez-Navarro, S. Cecioni, S. Vidal, K. Buffet, M. Durka, S. P. Vincent, *Chem. Commun.* **2010**, *46*, 3860; b) J. Luczkowiak, A. Muñoz, M. Sánchez-Navarro, R. Ribeiro-Viana, A. Ginieis, B. M. Illescas, N. Martín, R. Delgado, J. Rojo, *Biomacromolecules* **2013**, *14*, 431; c) A. Muñoz, D. Sigwalt, B. M. Illescas, J. Luczkowiak, L. Rodríguez-Pérez, I. Nierengarten, M. Holler, J.-S. Remy, K. Buffet, S. P. Vincent, J. Rojo, R. Delgado, J.-F. Nierengarten, N. Martín, *Nat. Chem.* **2016**, *8*, 50; d) A. Muñoz, B. M. Illescas, J. Luczkowiak, F. Lasala, R. Ribeiro-Viana, J. Rojo, R. Delgado, N. Martín, *J. Mat. Chem. B* **2017**, *5*, 6566; e) J. Ramos-Soriano, A. Pérez-Sánchez, S. Ramírez-Barroso, B. M. Illescas, K. Azmani, A. Rodríguez-Fortea, J. M. Poblet, C. Hally, S. Nonell, D. García-Fresnadillo, J. Rojo, N. Martín, *Angew. Chem., Int. Ed.* **2021**, *60*, 16109; f) B. M. Illescas, J. Rojo, R. Delgado, N. Martín, *J. Am. Chem. Soc.* **2017**, *139*, 6018.

[12] J. Ramos-Soriano, J. J. Reina, B. M. Illescas, N. De La Cruz, L. Rodríguez-Pérez, F. Lasala, J. Rojo, R. Delgado, N. Martín, *J. Am. Chem. Soc.* **2019**, *141*, 15403.

[13] J. Ramos-Soriano, B. M. Illescas, A. Pérez-Sánchez, R. Sánchez-Bento, F. Lasala, J. Rojo, R. Delgado, N. Martín, *Int. J. Mol. Sci.* **2022**, *23*, 5083.

[14] a) J. Cabrera-González, J. Soriano, R. Conway-Kenny, J. Wang, Y. Lu, J. Zhao, C. Nogués, S. M. Draper, *Biomat. Sci.* **2019**, *7*, 3287; b) D. Yao, X. Zhang, O. Mongin, F. Paul, C. O. Paul-Roth, *Chem. -Eur. J.* **2016**, *22*, 5583.

[15] a) H. Isobe, K. Cho, N. Solin, D. B. Werz, P. H. Seeberger, E. Nakamura, *Org. Lett.* **2007**, *9*, 4611; b) I. Nierengarten, J.-F. Nierengarten, *Chem. Rec.* **2015**, *15*, 31.

[16] a) A. Hirsch, O. Vostrowsky, *Eur. J. Org. Chem.* **2001**, *2001*, 829; b) J.-F. Nierengarten, *Chem. Commun.* **2017**, *53*, 11855.

[17] M. Sánchez-Navarro, A. Muñoz, B. M. Illescas, J. Rojo, N. Martín, *Chem. -Eur. J.* **2011**, *17*, 766.

[18] a) A. R. Mcdonald, N. Franssen, G. P. M. Van Klink, G. Van Koten, *J. Organomet. Chem.* **2009**, *694*, 2153; b) S. M. Aly, H. Guernon, B. Guérin, P. D. Harvey, *J. Porphyr. Phthalocyanines* **2011**, *15*, 871.

[19] Y. Rio, M. Salomé Rodríguez-Morgade, T. Torres, *Org. Biomol. Chem.* **2008**, *6*, 1877.

[20] a) A. Macchioni, G. Ciancaleoni, C. Zuccaccia, D. Zuccaccia, *Chem. Soc. Rev.* **2008**, *37*, 479; b) Y. Cohen, L. Avram, L. Frish, *Angew. Chem., Int. Ed.* **2005**, *44*, 520.

[21] K. F. Morris, C. S. Johnson Jr, *J. Am. Chem. Soc.* **1992**, *114*, 3139.

[22] O. Engström, A. Muñoz, B. M. Illescas, N. Martín, R. Ribeiro-Viana, J. Rojo, G. Widmalm, *Org. Biomol. Chem.* **2015**, *13*, 8750.

[23] a) M. P. Lenza, I. Oyenarte, T. Diercks, J. I. Quintana, A. Gimeno, H. Coelho, A. Diniz, F. Peccati, S. Delgado, A. Bosch, M. Valle, O. Millet, N. G. A. Abrescia, A. Palazón, F. Marcelo, G. Jiménez-Osés, J. Jiménez-Barbero, A. Ardá, J. Ereño-Orbea, *Angew. Chem., Int. Ed.* **2020**, *59*, 23763; b) R. Amraei, W. Yin, M. A. Napoleon, E. L. Suder, J. Berrigan, Q. Zhao, J. Olejnik, K. B. Chandler, C. Xia, J. Feldman, B. M. Hauser, T. M. Caradonna, A. G. Schmidt, S. Gummuluru, E. Muhlberger, V. Chitalia, C. E. Costello, N. Rahimi, *ACS Cent. Sci.* **2021**, *7*, 1156.

[24] a) P. Valverde, S. Delgado, J. D. Martínez, J.-B. Vendeville, J. Malassis, B. Linclau, N.-C. Reichardt, F. J. Cañada, J. Jiménez-Barbero, A. Ardá, *ACS Chem. Biol.* **2019**, *14*, 1660; b) K. Pederson, D. A. Mitchell, J. H. Prestegard, *Biochemistry* **2014**, *53*, 5700.

[25] J. Aretz, H. Baukmann, E. Shanina, J. Hanske, R. Wawrzinek, V. A. Zapol'skii, P. H. Seeberger, D. E. Kaufmann, C. Rademacher, *Angew. Chem. Inter. Ed.* **2017**, *56*, 7292.

[26] P. Mateos-Gil, A. Tsortos, M. Vélez, E. Gizeli, *Chem. Commun.* **2016**, *52*, 6541.

[27] a) J. Geurtsen, N. N. Driessen, B. J. Appelmelk, in *Microbial Glycobiology* (Eds.: O. Holst, P. J. Brennan, M. v. Itzstein, A. P. Moran), Academic Press, San Diego **2010**, 673; b) H. Feinberg, R. Castelli, K. Drickamer, P. H. Seeberger, W. I. Weis, *J. Biol. Chem.* **2007**, *282*, 4202.